

Optically Driven Janus Micro Engine with Full Orbital Motion Control

David Bronte Ciriza,^{1, a)} Agnese Callegari,² Maria Grazia Donato,¹ Berk Çiçek,³
Alessandro Magazzù,¹ Iryna Kasianiuk,^{3,4} Denis Kasianiuk,^{3,4} Falko Schmidt,⁵ Antonino
Foti,¹ Pietro G. Gucciardi,¹ Maurizio Lanza,¹ Luca Biancofiore,^{3,4, b)} and Onofrio M.
Maragò¹

¹⁾*CNR-IPCF, Istituto per i Processi Chimico-Fisici, I-98158, Messina,
Italy*

²⁾*Department of Physics, University of Gothenburg, SE-41296, Gothenburg,
Sweden*

³⁾*Department of Mechanical Engineering, Bilkent University, TR-06800, Ankara,
Turkey*

⁴⁾*UNAM - National Nanotechnology Research Center and Institute of
Materials Science & Nanotechnology, Bilkent University, 06800 Ankara,
Turkey*

⁵⁾*Nanophotonic Systems Laboratory, Department of Mechanical and Process Engineering,
ETH Zurich, CH-8092, Zurich, Switzerland*

(Dated: 12 May 2023)

Microengines have shown promise for a variety of applications in nanotechnology, microfluidics, and nanomedicine, including targeted drug delivery, microscale pumping, and environmental remediation. However, achieving precise control over their dynamics remains a significant challenge. In this study, we introduce a microengine that exploits both optical and thermal effects to achieve a high degree of controllability. We find that in the presence of a strongly focused light beam, a gold-silica Janus particle becomes confined at the equilibrium point between optical and thermal forces. By using circularly polarized light, we can transfer angular momentum to the particle breaking the symmetry between the two forces and resulting in a tangential force that drives directed orbital motion. We can simultaneously control the velocity and direction of rotation of the particle changing the ellipticity of the incoming light beam, while tuning the radius of the orbit with laser power. Our experimental results are validated using a geometrical optics model that considers the optical force, the absorption of optical power, and the resulting heating of the particle. The demonstrated enhanced flexibility in the control of microengines opens up new possibilities for their utilization in a wide range of applications, encompassing microscale transport, sensing, and actuation.

^{a)}brontecir@ipcf.cnr.it

^{b)}luca@bilkent.edu.tr

I. INTRODUCTION

Microengines have steadily gained popularity and become prevalent as effective tools for controlling processes on small scales¹. Their ability to convert energy into active motion makes them essential for nanotechnology applications such as generating precise fluid flows in microfluidic chips²⁻⁴, delivering drugs more efficiently in nanomedicine⁵⁻⁷, or for environmental remediation^{8,9}. Janus particles¹⁰, characterized by two distinct hemispheres with different physical properties, are the most widely used model system for microengines. Their inherently asymmetric design allows them to self-propel under various conditions. For instance, dielectric Janus particles can be designed with a metallic cap that generates a local, asymmetric heat profile under light exposure, resulting in its directed motion¹¹⁻¹⁵. While microengines are able to overcome random thermal fluctuations and exhibit directed motion, the lack of control over their dynamics is a significant limitation for their broader application.

Light is one of the most efficient approaches to induce and control the motion of microengines¹⁶⁻¹⁸. Although non-optical electric¹⁹ and magnetic fields²⁰ are also promising alternatives, light has distinct advantages such as high energy density, precise control over its position and time, and the ability to effectively transfer both linear and angular momentum²¹. Specifically, a highly focused laser beam can confine particles around the focal point through the exchange of momentum between light and particles, a technique known as optical tweezers²². Once confined, by transferring momentum to the particle, there are two main strategies for turning the trapped particle into a rotating microengine. Firstly, spin²³⁻²⁵ and/or orbital^{24,26,27} angular momentum can be transferred to the particle, generating a polarization or phase-dependent torque that drives orbital rotations. The direction of rotation can be controlled by adjusting the beam's polarization or phase gradients. Secondly, for asymmetric particles the scattering generates an optical torque^{21,28-30} where the direction of rotation is fixed by the scattering pattern (windmill effect) and determined by the particle's shape. This effect has also been observed for metal-dielectric Janus particles^{11,31}, highlighting the relevance of both light scattering and thermal effects¹¹.

Indeed, for light absorbing particles, not only momentum transfer but also energy absorption and consequent heating plays a key role in their dynamics, giving rise to more complex behaviours^{4,11-14,32-36}. Because of the combination of optical and thermal effects, microengines can show elevator-like motion¹³, elliptical³⁵, trochoidal¹² and circular orbits^{4,11,34}, can rotate at higher velocities³³, and present reconfigurable assemblies of multiple particles³⁷. This shows that

the integration of optical and thermal effects can induce a diverse range of dynamic behaviours. However, the controllability over these dynamic behaviours is very limited. For instance, unless the beam is continuously repositioned³², the direction of rotation is either fixed by a previously designed particle’s geometry³³ or is erratic and influenced by random thermal fluctuations^{4,11,34,35}. Thus, a more sophisticated scheme is required to simultaneously manipulate the direction of rotation and the angular velocity in order to enhance the control of microengines.

In this study, we combine the precise control obtainable via optical forces with the strong driving forces of thermal effects to realize a microengine that allows simultaneous control of its speed, radius, and direction of rotation using a single beam of light. Specifically, we investigate a gold-silica Janus particle trapped by a linearly polarized Gaussian beam at a distance from the beam’s center where the opposing optical and thermal forces balance. By switching to circularly polarized light, due to the transfer of the light’s spin angular momentum to the particle, the symmetry between both forces breaks inducing orbital rotations of the particle around the beam’s axis. We control the particle’s direction of rotation and angular velocity by tuning the beam’s ellipticity, showing that transitions between rotational and stationary states can be achieved within the same system. The experimental results are in agreement with an extended geometrical optics model that also considers the polarization of the light beam and enables the calculation of the optical power absorbed in the particle’s cap. Our findings delve into the complexities of light-matter interactions in thermally driven microengines, presenting new insights and paving the way for enhanced control and manipulation in the field of nanotechnology.

II. RESULTS AND DISCUSSION

In this study, we investigate a microengine driven by both optical and thermal effects and whose motion we can precisely control by adjusting the power and polarization of the incident light beam. The microengine consists of a gold-capped silica Janus particle fabricated by sputtering a 10 nm-thick gold layer on top of a $3\ \mu\text{m}$ diameter silica particle (Figure 1). The particle’s gold facet is optically thin enough to not drastically change its optical properties and thus its trapping capabilities but thick enough to induce thermal temperature gradients under light illumination (see Methods-Numerical Model). The beam shines from below (red arrow in Figure 1(a)) and the focal spot is located at a distance $h = 8\ \mu\text{m}$ above the particle (bright spot at the top of Figure 1(a)). When the beam is circularly polarized (white spiral in Figure 1(a)), the Janus particle performs

orbital rotations at almost constant speed v around the beam's center. The particle's motion is recorded via digital video microscopy at 20 fps and tracked with customized Python routines. During its motion, the particle's gold-cap always faces inwards (vector n pointing away from the cap in Figure 1(a)) and in the presence of circular polarization is slightly misaligned (θ) with the local Poynting vector (S) of the laser beam, see angle θ between the xy -projections of n and S (yellow and green dashed lines respectively). We observe this behaviour for various distances between particle and focal spot in the range $6 \leq h \leq 10 \mu\text{m}$, whereas the particle can not be trapped for $h \leq 6 \mu\text{m}$ or does not rotate for $h \geq 10 \mu\text{m}$. We find that the microengine is driven by both optical and thermal effects, and can be precisely controlled by adjusting the power and polarization of the incident light beam. Through both experimental and numerical analysis, we explore the dynamics of the microengine under varying light power and polarization conditions.

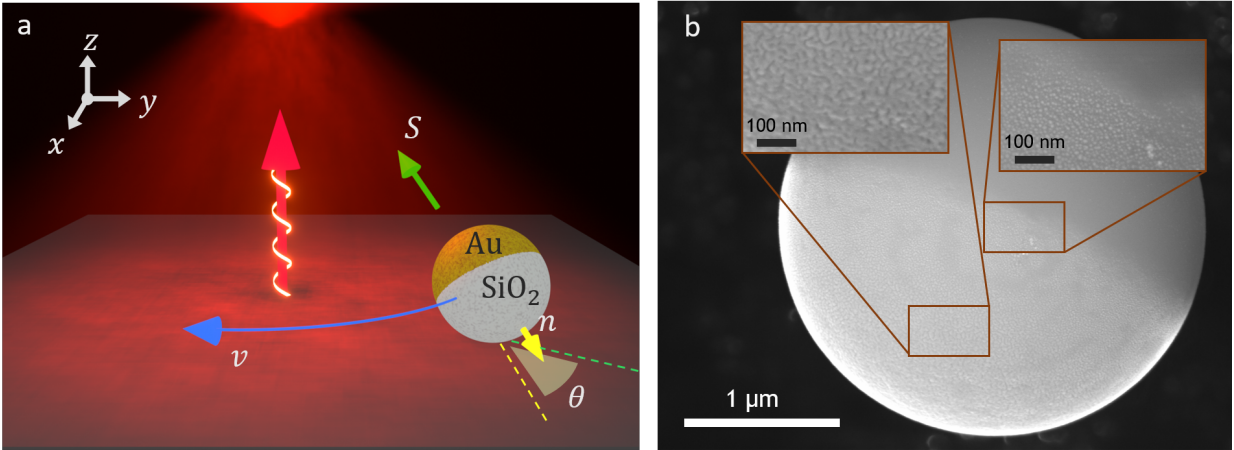


FIG. 1. Orbital motion of Janus particle under circularly polarized light. a) Schematic of the orbital motion of a gold-capped Janus particle made of SiO_2 under a circularly polarized focused beam (red arrow with white spiral illustrating the direction and polarization of the light beam). The particle is constantly rotating at speed v (blue arrow) around the center of the beam $8 \mu\text{m}$ below its focal point (red spot on the top). The particle's orientation is slightly tilted at angle θ , which indicates the misalignment between the xy -projections of the cap orientation (yellow arrow, n) and the local Poynting vector (green arrow, S). b) SEM images of the fabricated Janus particles. Insets show specific regions of the particle, where the left inset show deposited gold layer and the right inset the transition from the gold cap to the SiO_2 particle.

A. Motion as a function of laser power

When the light is circularly polarized, the Janus particle performs continuous circular orbits (Figure 2(a)). Upon increasing the power of the light beam we observe that both the orbital radius (ρ) and the confinement of the particle are increasing (Figure 2(b)). At low power ($P = 6$ mW) the Janus particle is mostly located in close proximity to the beam center ($\rho = 2.4 \pm 0.6 \mu\text{m}$) and the distribution of radial positions has a large standard deviation. At intermediate powers ($P = 16$ mW) the radius of motion increases and the radial confinement is enhanced, resulting in a narrower radial distribution. The average radial position peaks at the maximum power of our laser $P = 34$ mW with $\rho = 7.5 \pm 0.4 \mu\text{m}$, showing a well defined circular trajectory. Plotting the probability distribution of the radial positions we find Gaussian-like profiles from which we obtained ρ , see Figure 2(c). Applying the equipartition theorem we can relate the width of the Gaussian profile to the trap stiffness as: $k_\rho = k_B T / \sigma^2$. We find that the stiffness values grow from $k_\rho = 11 \pm 3$ nN/m for $P = 6$ mW to $k_\rho = 20 \pm 7$ nN/m for $P = 16$ mW and peak for $P = 30$ mW with $k_\rho = 38 \pm 7$ nN/m. Although the stiffness values we obtained are about two orders of magnitude lower than those reported for similarly sized uncoated silica particles trapped at the focus of a laser beam²¹, they are sufficient to prevent the particle from escaping.

Next, we fully characterize the dependence of the particle's motion on laser power for its change in orbital radius ρ , angular speed ω , and linear speed v . We find that ρ increases non-linearly reaching the maximum radius at the maximum power ($P = 34$ mW, Figure 2(d)). Although ω decreases slightly (between 1.6 ± 0.2 and 1.3 ± 0.1 rad/s, Figure 2(e)) the linear speed v increases significantly (from 3.8 ± 1.2 to $9.5 \pm 0.6 \mu\text{m/s}$) with increasing laser power (Figure 2(f)). While the decrease in angular velocity with laser power is modest, the strong power dependence of the particle's radial distance is ultimately responsible for the observed increase in linear velocity.

Similarly shaped orbits such as the exhibited by our proposed microengine have been previously reported in the literature^{11,13,34}. However, our microengine offers distinct advantages in terms of controllability. While previous systems with Janus particles in water showed sudden jumps in equilibrium position when varying laser power for circular orbits¹¹ as well as for elevator-like motion¹³ our microengine exhibits a smooth dependence of the orbital radius ρ with power. A similar power dependence of ρ has been reported for optically heated spheres at a water-air interface (ranging between 3 and 11 μm)³⁴. Moreover, an advantage of our system is the presence of continuous and predictable rotations, which contrasts with the orbiting microengines reported in

previous studies^{11,34} that rotate in unpredictable directions and can change the direction of rotation randomly.

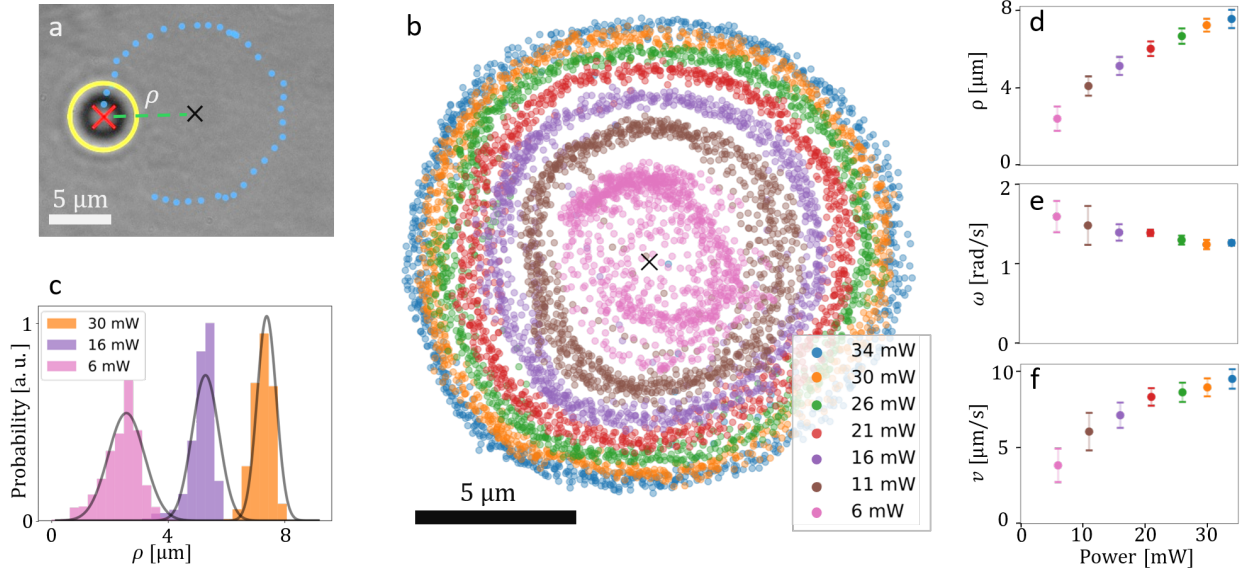


FIG. 2. Janus particle motion dependence on laser power P . a) Bright-field image of a tracked Janus particle (yellow outline) with center-of-mass position (red cross) rotating around the center of the beam (marked by black cross) at a distance ρ (green dashed line) with its circular trajectory (blue dotted line) during 3.5 s. b) Recorded positions of the particle orbiting around the center of the beam (black cross) for different incident powers P for 50 s-long trajectories. c) Probability distribution of ρ for three different powers ($P = 6, 16$ and 30 mW) and fitted with a Gaussian function. From the Gaussian fit, applying the equipartition theorem we obtain the trap stiffness. d) Average radius ρ , e) average angular velocity ω , and f) average linear velocity v of the trajectories as a function of laser power. The error bars correspond to the standard deviation for 5 measurements of 10 s each.

B. Motion as a function of light polarization

Transfer of angular momentum can induce rotation of particles around their own axis²⁵. In our experiment, circularly polarized light induces a spinning rotation of the particle around its z -axis that breaks the symmetry between optical and thermal forces acting on it and thus induces its directional orbital motion. This motion can be stopped or reversed by changing the polarization state of the light, see Figure 3(a-c). When exposed to linearly polarized light, the particle remains

confined to a specific distance ρ from the center of the beam where it diffuses randomly due to Brownian motion, see Figure 3(b). When applying circularly polarized light, the direction of rotation is entirely determined by the polarization direction of the circularly polarized light, and can be reversed by switching between clockwise and anticlockwise circular polarization (Figs. 3 (a,c)). From the recorded video frames in Figs. 3 (a-c) we observe the gold-coated side of the Janus particle (the darkest region in transmission microscopy) facing always radially inwards to the center of the beam (yellow arrows represent the orientation vector n in Figure 1(a)). Note that for circular polarization the orientation vector n is not aligned with the position vector (green dashed line in Figure 3(a,c)) but is slightly tilted, which results in the breaking of symmetry that generates the tangential force (F_{tan}) responsible for its motion.

Although the particle's direction of rotation is determined by the polarization of the beam, the orbit and radius of motion are independent of polarization and are solely determined by the power (as discussed in the previous section). Figure 3(d) shows the particle's positions and the direction of motion for 60 s trajectories (each point represents 1 s time steps). Pink and blue points represent different senses of circularly polarized light whereas orange points indicate linearly polarized light. The particle is located at a distance ρ of around $7 \mu\text{m}$ and eventually closes a loop in approximately 6 s. The erratic Brownian motion observed for linear polarization (orange points in the upper right corner) where the particle remains at the same location and diffusing due to Brownian motion, stands in contrast to the well-defined directional motion observed for circular polarization (blue and pink points).

Additional control can be gained by also adjusting the velocity and direction of rotation using elliptical polarization, as demonstrated in Figure 4. We have previously shown that changing laser power affects, both, the microengine's velocity and the radius of rotation, see Figure 2(d,f). However, adjusting the ellipticity of the light allows further velocity tuning without affecting the radius. Completely circularly polarized light yields the highest values of the angular velocity (ω), see $\phi = \pm\pi/4$ in Figure 4, where ϕ is the angle between the polarization plane of the linearly polarized and the fast axis of the $\lambda/4$ wave plate. Furthermore, the experimental velocities match the theoretical dependence on $\sin(2\phi)$, see Figure 4. Note that the standard deviations of the angular velocities are three times larger for intermediate elliptical polarizations than for circular polarization. We attribute this to asymmetries in the beam profile that create energy barriers that are more difficult to overcome when the tangential force F_{tan} is lower, resulting in a less homogeneous motion. The slight difference (30%) between the experimental maximum velocity for clockwise and

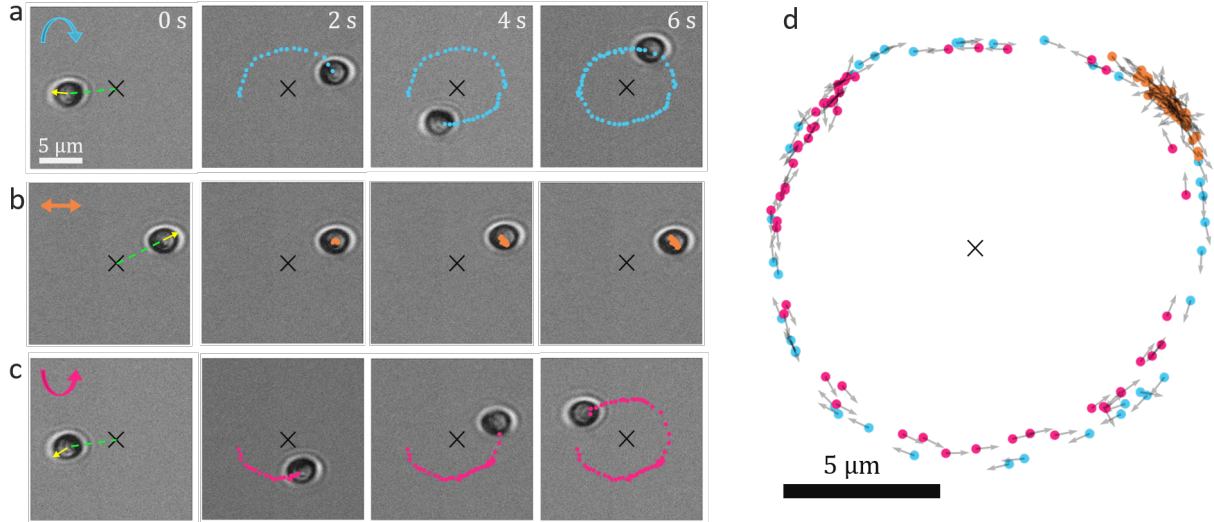


FIG. 3. Motion of a Janus particle as a function of light polarization. a-c) The particle is shown at $t = 0, 2, 4$ and 6 s, the plotted points correspond to previous positions at 0.1 seconds intervals. The black cross indicates the centre of the beam and the yellow arrows in the initial frame represent the orientation vector n as illustrated in Figure 1(a). The green dashed lines show the direction of the local Poynting vector. a) Light circularly polarized clockwise induces clockwise rotation with more than a full orbit completed after 6 s. b) Light linearly polarized keeps the same particle at the same radius diffusing with no directed motion. c) Light circularly polarized anticlockwise induces anticlockwise rotation with almost a full orbit completed after 6 s. d) Positions (points) and direction of motion (arrows) of the particle for linearly polarized light (orange), circularly polarized light in clockwise (blue), and anticlockwise directions (pink). Positions are plotted every second for a 60 s-long trajectory.

anticlockwise polarization is likely due to differences in the transmission of optical elements such as mirrors and dichroic beam splitters that result in slightly lower power for clockwise polarization.

Although there exist other microengines capable of producing closed orbits^{4,11,34}, they are unable to be stopped at a specific location within their trajectory without minimizing the power and returning to the center of the beam. Our microengine, in contrast, offers complete flexibility in terms of orbital direction, the ability to halt at any distance, and even reverse its trajectory, therefore setting a new standard in controlling microsystems that are typically dominated by random fluctuations. The precision of control demonstrated by our proposed microengine, achieved through the ellipticity of the incoming beam, is only comparable to microengines that rely on transferring angular momentum between particles and light^{24,26,38}. However, our microengine distinguishes

itself by enabling control at various distances from the beam center, rather than being limited to a single focal point.

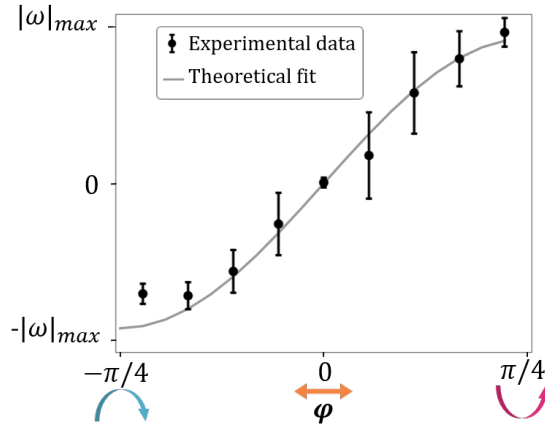


FIG. 4. **Angular velocity as a function of the ellipticity of the light.** The solid line indicates the theoretical dependence on $\sin(2\phi)$. The experimental error bars correspond to the standard deviation for 5 measurements of 10 seconds each.

C. Numerical study

We are performing numerical simulations to deeper investigate the individual contributions of optical and thermal forces. By studying the problem numerically we also find that the interplay between optical and thermal forces generates a stable equilibrium position at a specific distance ρ from the center of the beam. The model, by considering the geometrical optics approximation³⁹, computes both the exchange of momentum between light and particle (generating optical forces²¹) and the absorption and consequent heating of the gold cap (generating thermal forces⁴⁰). While the optical force draws the particle towards the center, the thermal force, caused by the difference in temperature between the gold (inner part) and silica (outer part), pushes the particle away. The combined effect of the opposing forces creates a force that cancels out at a distance ρ , resulting in an equilibrium point, see Figure 5(a). Furthermore, the total force has a negative slope at the point where the opposing optical and thermal forces are balanced, see the inset of Figure 5(a), leading to the formation of a stable equilibrium point. If the particle moves further away, it will experience a negative force that will attract the particle back towards the stable equilibrium. On the contrary, if the particle approaches the center, it will experience a positive force pushing it away. For small displacements from the equilibrium position, the total force F_{tot} can be approximated as

a harmonic potential ($F_{\text{tot}} = -k_{\rho} \rho$), with the stiffness of the potential k_{ρ} being determined by the slope of the force in the proximity of the equilibrium point, see dashed red line in Figure 5(a).

We find that our numerical analysis is consistent with our experimental results demonstrating that the orbital radius of the Janus particle increases with power, see Figure 5(b). While the forces are increasing with power, their dependence is non-linear thereby shifting the equilibrium position. If, both, optical and thermal forces grew linearly with the power, the stiffness would increase linearly but the equilibrium position wouldn't shift, as the forces would still balance at the same point, which is in contrast to experimental observations. In our model, optical forces are considered to scale linearly with the power whereas the thermal force introduces non-linearities, see Eq. 4 and Eq. 9 respectively. In our simulations, we observe a change in equilibrium position from $3.0 \pm 0.7 \mu\text{m}$ at 10 mW to $9.0 \pm 0.5 \mu\text{m}$ at 35 mW (experiments show ranges from 2.4 ± 0.6 to $7.5 \pm 0.4 \mu\text{m}$) and the stiffness grows from 9 nN/m to 16 nN/m, respectively (experiments show growth from 11 ± 3 to 38 ± 7 nN/m), which is in good agreement with the experimental results. Higher powers push the particle further away while increasing its radial confinement as consistent with previous observations.

Under circularly polarized light, the polarization of the light causes the particle to spin around its own z -axis. The force acting in the tangential direction F_{tan} is due to the symmetry breaking between the optical and thermal forces (the optical force pulling the particle towards the center of the beam and the thermal force pushing it from the gold to the silica part). More precisely, in the presence of circularly polarized light, the orientation of the cap n is not exactly the one of the local Poynting vector S , but slightly tilted due to an additional small azimuthal rotation by transfer of angular momentum that breaks the mirror symmetry of the configuration. This creates a steady tangential force F_{tan} that keeps the particle rotating in its circular orbit. As we observe continuous rotations, we know that the tangential component of the thermal force should be equal to the drag force: $F_{\text{tan}} = \gamma v$, where γ is the viscous coefficient and v is the speed of the particle. The numerical model allows us to also determine the radial component of the thermal force (As the radius remains constant, it must have same magnitude and opposite in direction to the optical force). Knowing both, radial and tangential components of the thermal force, we can estimate the required rotation θ of the particle around the vertical direction to give the expected tangential force. We find this angle θ to be around 10° for circularly polarized light. On the other hand, When the polarization is linear (see Supplementary Figure 10), the cap is aligned with the local Poynting vector such that the absence of the tangential force does not induce steady rotation.

Our Brownian dynamics simulations (see Methods-Numerical Model) also confirm that the particle remains confined at a given radius ρ that increases with power from $3.3 \pm 0.9 \mu\text{m}$ at 10 mW up to $9.1 \pm 0.6 \mu\text{m}$ at 35 mW, see Figure 5(c), which is consistent with both experimental and theoretical results. Additionally, the simulations verify that the radial confinement does also depend on the power, with the trajectory for higher powers being less spread than that for lower ones, see Figure 5(c). In Figure 5(d) we show simulations where different ellipticities of the incoming light such as in experiments have been considered. In particular, we plot the results for circularly polarized light in both orientations (blue and pink points) and for linearly polarized light (orange points). As for our experimental results (see Figure 3(d)), in the case of linear polarization the particle remains around the same location and only diffuses, which stands in contrast to the well-defined directional motion observed for circular polarization.

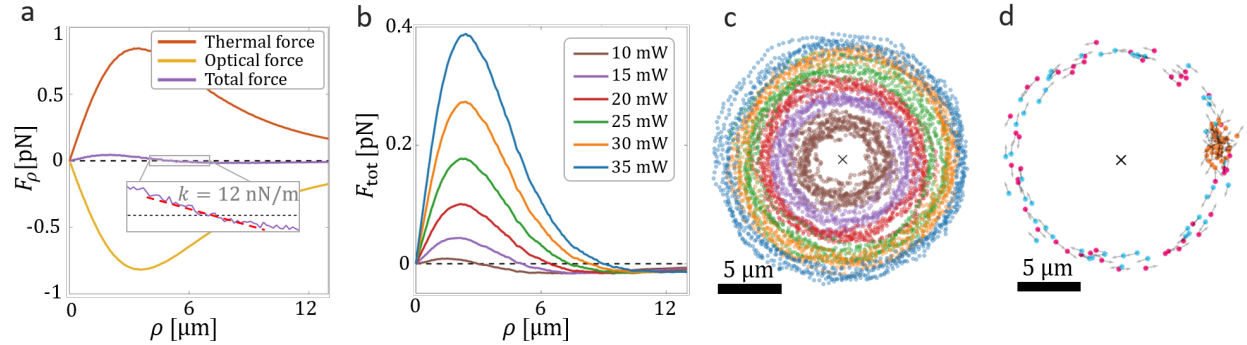


FIG. 5. Numerical study of the microengine. a) Thermal, optical, and total force in the radial direction as a function of the radius for a power of 15 mW. The equilibrium point is at $\rho = 5.1 \pm 0.6 \mu\text{m}$ and the stiffness is 12 nN/m. b) Total force exerted on the particle as a function of ρ for different powers. Both the equilibrium position and the stiffness increase with the power. c) Simulation of the dynamics of the Janus particle for a 50 seconds trajectory when illuminated with different powers and d) simulation of the dynamics of the particle under anticlockwise circularly polarized light (pink), linearly polarized light (orange) and clockwise circularly polarized light (blue). The black crosses represent the center of the beam. The parameters of the plots c) and d) are identical to the ones of Figure 2 and Figure 3.

III. CONCLUSION

In this study, we have introduced a highly controllable microengine by combining both optical and thermal effects. We demonstrated that a $3\ \mu\text{m}$ gold-silica Janus particle can be confined at a specific distance from the center of a highly focused beam, with the gold side facing inwards. The balance between optical forces, which pull the particle towards the high intensity region, and thermal forces, which push it away from the same region, is responsible for this confinement. Remarkably, the equilibrium position can be fine-tuned by adjusting the beam power. Furthermore, we showed that circularly polarized light can transfer spin angular momentum from the light to the particle, breaking the mirror-symmetry of the system and inducing a moon-like rotation (orbital motion of the particle around the beam's axis with the gold side towards the center of the beam). The speed and the orientation of this rotation can be precisely controlled by varying the ellipticity of the light. Our experimental findings have been validated by a numerical model that matches our observations and provides further insights into the intrinsic properties of the system. Overall, the high degree of control we have achieved with this microengine opens up new possibilities in a wide range of applications, from microscale transport to sensing and actuation.

IV. METHODS

A. Janus particles

The fabrication of the Janus particles (diameter $3\ \mu\text{m}$) made of silica (SiO_2) and half coated with gold (Au) splits into three different steps. The first one consists of obtaining a crystalline monolayer of silica spheres on the glass surface. Starting from a solution of silica spheres in water, we deposit the droplet on the glass, and when the solvent evaporates we obtain a monolayer of particles on the substrate. We find the best structures when covering the substrate with a Petri-dish and keeping it at a temperature of 19°C until the sample dries. The second step consists of coating one half of the particles' surface with a 10-nm thick layer of gold. For this, we employ the thermal evaporation technique, which evaporates the metal and condenses it on the particles surface at high vacuum conditions. To improve the adhesion of gold to silica, we added a 2 nm layer of Titanium before adding gold. Third and last, to release the particles in solution, we immerse the substrate in water and sonicate for 5 seconds (SONICA, 1200M). SEM micrographs were collected by a Quanta 450 (FEI, Hillsboro, OR, USA) with a large-field detector (LFD) and

an accelerating voltage of 20 kV in high vacuum (1^{-6} mbar).

B. Experimental setup

To prepare the sample chamber, a small amount of Janus particles in aqueous suspension (15 – 20 μ l) is drop casted on a clean microscope slide and then covered with a coverslip. The obtained chamber is sealed with nail polish to avoid evaporation during measurements. The light source for the optical tweezers is a laser diode source (Thorlabs DL8142-201) at 830 nm wavelength. After passing through a couple of anamorphic prisms and an optical isolator, the laser beam is expanded to overfill the back aperture of a high numerical aperture objective (Olympus, Uplan FLN 100X, NA=1.3), aiming at obtaining a diffraction-limited spot approximately 600 nm in diameter. Laser power at the objective is varied in the range between 5 and 35 mW. A $\lambda/4$ wave plate, placed in the beam path, is used to control the light polarization state. The relative position between the chamber and the focus of the beam is controlled using a piezoelectric stage (Mad City Labs NANO-LP200). The focal spot is located 8 μ m above the substrate while the motion of the particle takes place directly on top of the substrate. The particle images are taken in transmission with a CCD camera and are calibrated by imaging a microscope slide ruler. Tracking of the particle dynamics follows standardized digital video microscopy techniques and has been implemented in home-made Python codes. See Supplementary Figure 6 for an schematic of the experimental set up.

C. Numerical model

The interaction of the Janus particle with the focused Gaussian optical beam is described in the geometrical optics approximation^{39,41}: the beam is represented by an appropriate set of rays that, impinging on the Janus particle surface, are reflected, transmitted, and, when hitting the gold-coated spherical cap, also partially absorbed, see Supplementary Figure 7. While each ray is undergoing this infinite series of scattering events, it exchanges linear and angular momentum with the particle and therefore applies an optical force and torque. Additionally, the particle's metallic cap absorbs some of the incident light thereby increasing its temperature locally around the equilibrium point $\approx 5 - 10$ K. As the particle is immersed in solution, the temperature of the water in close proximity to the cap increases too: this asymmetry induces a temperature gradient

across the particle. As fluids typically move from cold to hot regions, the particle experiences a slip flow in the opposite direction, inducing thermophoretic (F_{thp}) motion of the particle¹⁵. Moreover, the temperature increase in the volume of water close to the particle induces a volume expansion of the water (F_{exp}). This causes an unbalanced force towards the non-expanding volume region (i.e. the “cold” side of the Janus particle). In practice, the particle feels a force proportional to the increased water volume, propelling the particle towards its cold end, See Supplementary Figure 8.

In agreement with experimental findings¹³ and with symmetry arguments, we assume that, in the case of a Janus particle with a hemisphere coated by a thin gold layer, the optical torque induced by geometrical scattering stably orients the particle such that its gold cap is aligned along the local Poynting vector S of the beam impinging on the particle, see Figure 1(a). Also, the combination of particle size ($3\ \mu\text{m}$) with the proximity to a planar boundary determines that the orientation of the particle is not very much affected by the Brownian noise, as the relaxation time of the rotational dynamics is significantly longer than the one in bulk in the order of magnitude of about 20s. In our dynamics simulation, hence, we consider the degrees of freedom related to the position of the particle center only, the orientation in each point defined by the local Poynting vector S , see Supplementary Figure 9.

From our main experimental observations we saw that elliptically polarized light induces orbital motion of the particle around the beam axis. We can simulate this by introducing a polarization dependent torque in our model. The Brownian dynamics equations for our particle, transposed already in the finite difference formalism, read as:

$$\left\{ \begin{array}{l} \Delta\rho = \frac{D_{\text{transl}}}{k_{\text{B}}T} F_{\rho,\text{tot}} \Delta t + \sqrt{2D_{\text{transl}} \Delta t} W_{\rho}, \\ \Delta s = \frac{D_{\text{transl}}}{k_{\text{B}}T} F_{s,\text{tot}} \Delta t + \sqrt{2D_{\text{transl}} \Delta t} W_s, \\ \Delta\psi = \frac{D_{\text{rot}}}{k_{\text{B}}T} T_{z,\text{pol}} \Delta t, \end{array} \right. \quad (1)$$

where ρ is the radial coordinate from the center of the beam and s is the coordinate in the tangential direction, oriented in the sense of positive angles (i.e., obtained from $\hat{\rho}$ and the direction of the beam propagation axis \hat{z} via $\hat{s} = \hat{z} \times \hat{\rho}$), and ψ is the azimuthal angle describing the orientation vector of the particle in the standard lab reference frame with basis unit vectors: $\hat{x}, \hat{y}, \hat{z}$.

The term $F_{\rho,\text{tot}}$ is the total force component along the radial direction $\hat{\rho}$, $F_{s,\text{tot}}$ is the component along the tangential direction \hat{s} , and $T_{z,\text{pol}}$ is the torque along the beam propagation axis direction \hat{z}

due to the amount of circular polarization of the light. The diffusion constants are D_{transl} and D_{rot} , which are related to the components D_{\parallel} , $D_{\text{rot},\perp}$ of the diffusion matrix of a spherical particle³⁶.

The total force is calculated as:

$$\mathbf{F}_{\text{tot}} = \mathbf{F}_{\text{opt}} + \mathbf{F}_{\text{thph}} + \mathbf{F}_{\text{exp}} + \mathbf{F}_{\text{weight}} + \mathbf{F}_{\text{buoyancy}} + \mathbf{F}_{\text{int}} \quad (2)$$

where \mathbf{F}_{opt} is the optical force due to the scattering of the rays on the particles, \mathbf{F}_{thph} is the thermophoretic force due to the slip flow of the thin layer of fluid in the proximity of the particle surface induced by the temperature gradient along the particle diameter (direction metallic cap-uncoated end), \mathbf{F}_{exp} is the force due to the volume expansion of the water, caused by the temperature increase, in the region near the cap, $\mathbf{F}_{\text{weight}}$ is the weight of the particle, $\mathbf{F}_{\text{buoyancy}}$ is the upwards force that the fluid applies to the particle because of its mass density, and \mathbf{F}_{int} is the interaction force with the bottom slide, that we assume to be short range and repulsive, representing a colloidal electrostatic interaction which decays exponentially with increasing distance between the particle and bottom slide preventing sticking. As the cap is oriented in the direction of the local Poynting vector, i.e., the coated cap faces the beam focus, while the uncoated particle hemisphere faces downwards and thus the bottom slide, the vertical component of the sum of all forces except for the electrostatic interaction with the substrate is directed downwards. Therefore, we assume that the substrate must always compensate the vertical forces with the right amount of repulsion, and the particle always remain close to the substrate at a given minimal distance from it (≈ 50 nm). For this reason, we do not include an explicit equation for the particle position in the vertical direction, See Supplementary Figure 10 for an schematic of the direction of the forces under different polarization conditions.

The expression for the different forces are given here below. The optical force is calculated in the standard way from the scattering, summing the contribution of the force due to the single rays³⁹:

$$\mathbf{F}_{\text{opt}} = \sum_m \mathbf{F}_{\text{ray}}^{(m)} \quad (3)$$

with

$$\mathbf{F}_{\text{ray}} = \frac{n_m P_i}{c} \hat{\mathbf{i}} - \frac{n_m P_r^{(1)}}{c} \hat{\mathbf{r}}_1 - \sum_{j=2}^{\infty} \frac{n_m P_t^{(j)}}{c} \hat{\mathbf{t}}_j, \quad (4)$$

The temperature increase is calculated while calculating the scattering, calculating the power absorbed by each single ray and summing it:

$$P_{\text{abs}} = \sum_m P_{\text{cap,ray}}^{(m)} \quad (5)$$

If we consider the cap isothermal, the temperature increase ΔT is

$$\Delta T = \frac{P_{\text{abs}}}{(2\pi + 4)\kappa_m R}, \quad (6)$$

where κ_m is the thermal conductivity of the medium and we can define a temperature gradient across the particle given by:

$$\nabla T = \frac{\Delta T}{\pi R}. \quad (7)$$

The thermophoretic velocity is expressed as $v_{\text{ph}} = -D_T \nabla T$ where D_T is the thermal diffusion coefficient⁴⁰. From v_{ph} we obtain $F_{\text{thph}} = \frac{k_B T}{D_{\text{transl}}} v_{\text{ph}}$. This force is assumed to push the particle in the n direction, from its coated cap to its uncoated end.

The magnitude force related to the volume expansion of the water when the temperature is increased (F_{exp}) is modelled as follows. We estimate a linear expansion coefficient c_L for the water between the base temperature (T) and the increased value of the temperature ($T + \Delta T$) as:

$$c_L = \frac{\rho_{\text{water}}(T)}{\rho_{\text{water}}(T + \Delta T)} - 1, \quad (8)$$

where $\rho_{\text{water}}(T)$ indicates the mass density of water at temperature T and we write:

$$F_{\text{exp}} = \alpha p_{\text{water}} c_L R^2, \quad (9)$$

where R is the radius of the particle, p_{water} is the hydrostatic pressure in the fluid, that we assume equal to the atmospheric pressure at sea level, and $\alpha = 0.003$ is a proportionality constant. This is a phenomenological, simplified model of the complex fluid dynamics occurring inside the fluid chamber, that are normally modelled using the Navier-Stokes equations. F_{exp} results from a force unbalance between the expanded water region (i.e., close to the gold cap) and the unexpanded water region (i.e., close to the silica half) and it is assumed to push the particle from the direction from its coated cap to its uncoated end.

The polarization torque is calculated summing the contribution of each ray impinging on the particle as:

$$T_{\text{pol}} = \sum_m \mathbf{T}_{\text{pol,ray}}^{(m)} \quad (10)$$

The contribution of each ray is modelled as proportional to the power absorbed on the first scattering event that involves the cap:

$$\mathbf{T}_{\text{pol,ray}}^{(m)} = \sigma \frac{P_{1,\text{abs,ray}}^{(m)}}{\omega} \hat{\mathbf{r}}_{1,\text{abs,ray}}^{(m)} \quad (11)$$

In the equation above, $\omega = 2\pi\nu$ is the angular frequency of the optical wavelength used for the laser beam, σ is a parameter between -1 and 1 describing the amount of circular polarization transported by each ray (where 0 corresponds to linear polarization), $P_{1,\text{abs,ray}}^{(m)}$ is the power that the m^{th} ray deposits on the cap the first time it hits the cap, and $\hat{\mathbf{r}}_{1,\text{abs,ray}}^{(m)}$ is the direction of the m^{th} ray when this event happens.

V. DATA AVAILABILITY

Data underlying the results presented in this paper are not publicly available at this time but may be obtained from the authors upon reasonable request.

VI. ACKNOWLEDGEMENTS

We acknowledge financial support from the European Commission through the MSCA ITN (ETN) Project “ActiveMatter”, Project Number 812780 and the Turkish National Research Agency (TUBITAK)-CNR Bilateral project 2020-2022 “Self-assembly of complex shaped active particles in controlled optical potentials”, TUBITAK project number 119N461. D.B.C, M.G.D., A.M., A.F., P.G.G. and O.M.M acknowledge funding from the European Union (NextGeneration EU), through the MUR-PNRR project SAMOTHRACE (ECS00000022) and PNRR MUR project PE0000023-NQSTI. FS acknowledges funding from the SNSF Postdoctoral Fellowship under grant agreement 209765.

VII. AUTHOR CONTRIBUTIONS

D.B.C. and M.G.D. performed the experiments. A.C., B.C., and D.B.C. prepared the numerical model, D.B.C. analyzed the data and wrote the initial draft. I.K. and D.K. fabricated the Janus particles. M.L. took the SEM images of the particles. L.B. and O.M.M. proposed and supervised the project. All authors discussed and commented on the results and on the manuscript text.

VIII. COMPETING INTERESTS

The authors declare no conflicts of interest.

IX. SUPPLEMENTARY INFORMATION

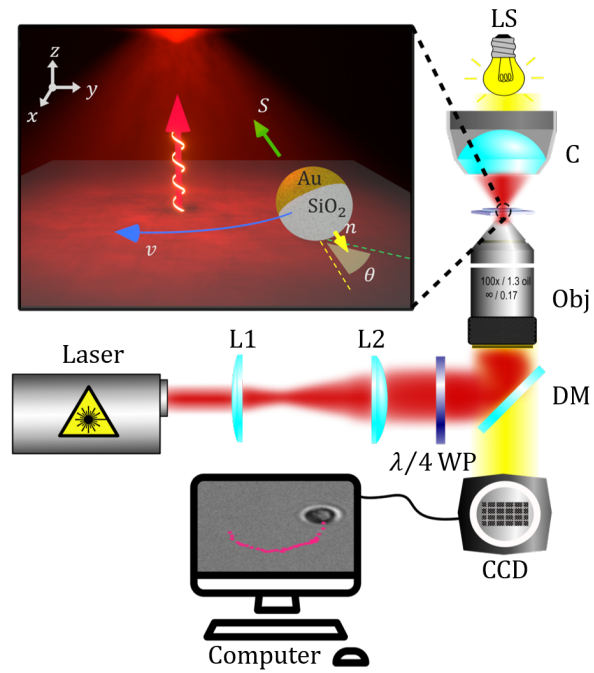


FIG. 6. **Schematic of the experimental set up.** The schematic includes the laser source, the two lenses (L1 and L2) that expand the beam, the $\lambda/4$ waveplate, the dichroic mirror (DM) that reflects the beam into the objective (Obj), the condenser (C), the illumination source (LS), and the computer that analyzes the images.

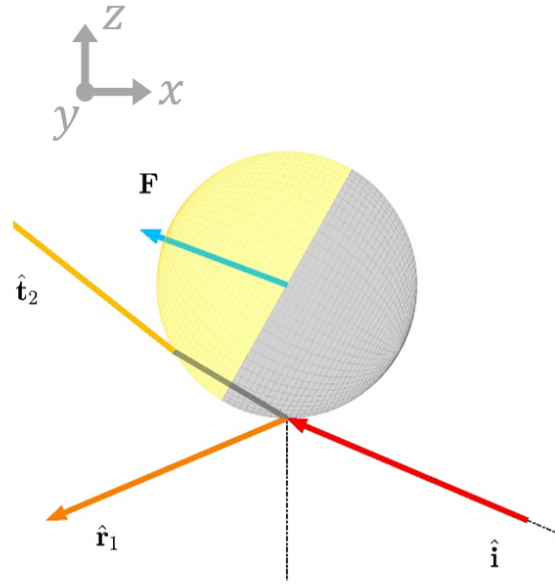


FIG. 7. **Schematic of a ray impinging on a Janus particle.** The ray \hat{i} reaches the particle and divides into a scattered ray \hat{r}_1 and a transmitted ray \hat{t}_2 . The change in linear momentum results in an applied force on the particle \mathbf{F}

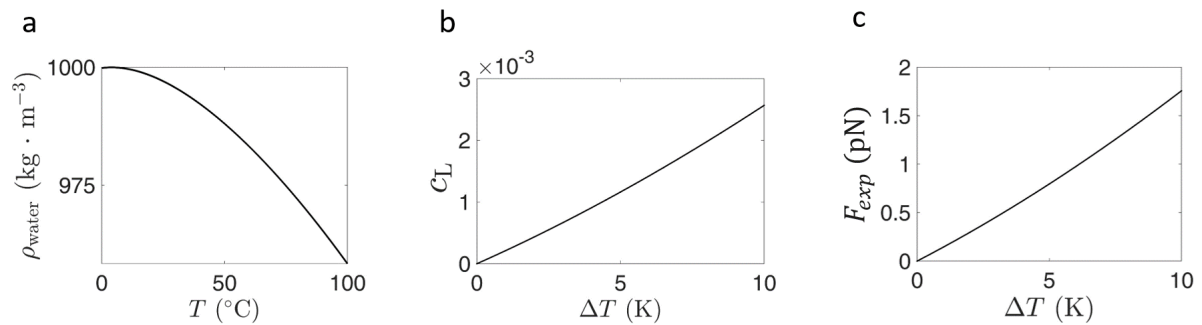


FIG. 8. **Density of water (ρ_{water}), linear expansion coefficient of water (c_L) and volume expansion force (F_{exp}) as a function of temperature.**

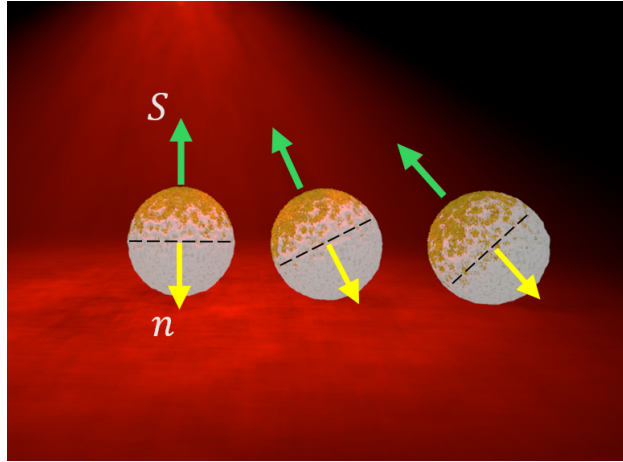


FIG. 9. **Orientation of the Janus particle for different radial positions under linearly polarized light.** The local Poynting vector of the focused beam (S , in green) is perpendicular to plane that contains the border between gold and silica and goes in the opposite direction to the the orientation vector (n , in yellow).

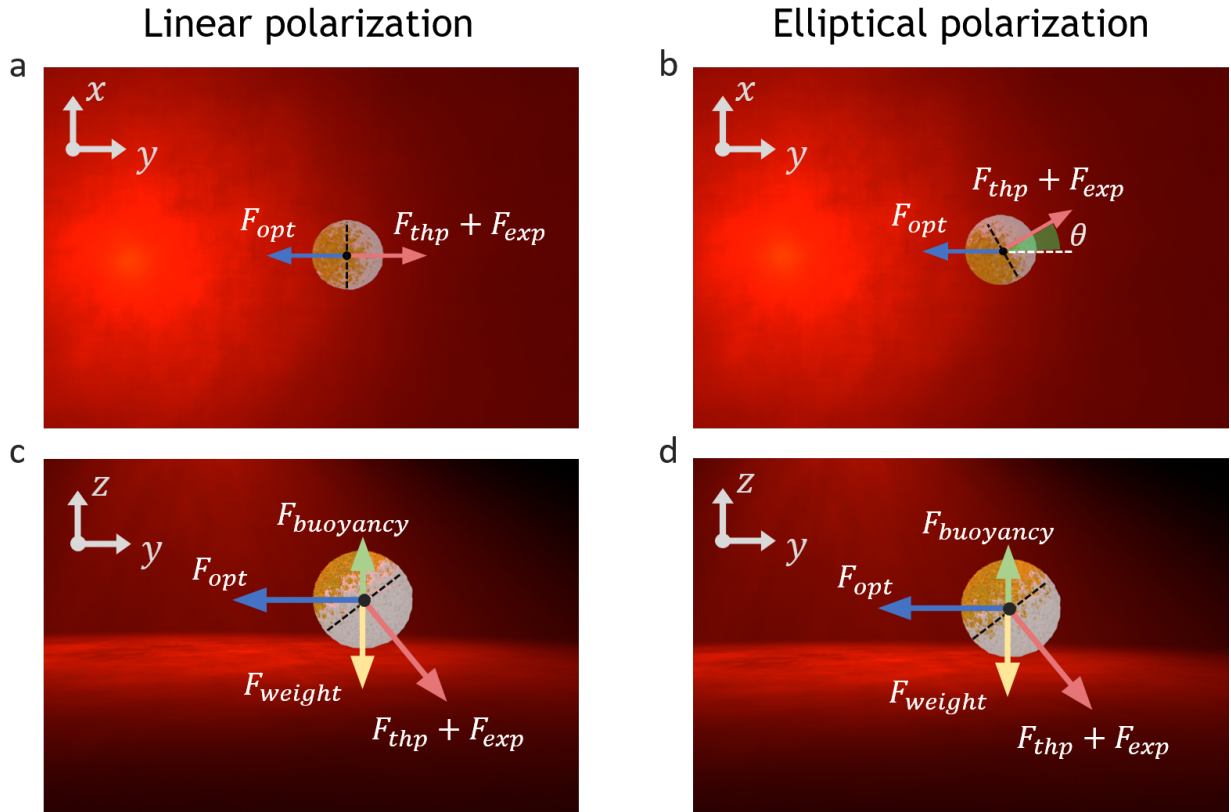


FIG. 10. **Forces acting on the Janus particle under different laser polarizations.** Forces acting on the Janus particle under linearly polarized light (a,c) and elliptically polarized light (b,d). Even though the optical force also has a scattering component in z direction, for simplicity here we present only the radial component. In (c), θ is the angle between the direction of the optical force (towards the center of the beam) and the direction of the thermal force (from gold to silica) that gives rise to the tangential force that drives the orbital motion.

REFERENCES

- ¹A. D. Fusi, Y. Li, A. Llopis-Lorente, T. Patiño, J. C. M. van Hest, and L. K. E. A. Abdelmohsen, “Achieving control in micro-/nanomotor mobility,” *Angewandte Chemie International Edition* **62**, e202214754 (2023).
- ²X.-F. Lin, G.-Q. Hu, Q.-D. Chen, L.-G. Niu, Q.-S. Li, A. Ostendorf, and H.-B. Sun, “A light-driven turbine-like micro-rotor and study on its light-to-mechanical power conversion efficiency,” *Applied Physics Letters* **101**, 113901 (2012).
- ³U. Bütaitė, G. M. Gibson, Y.-L. D. Ho, M. Taverne, J. M. Taylor, and D. B. Phillips, “Indirect optical trapping using light driven micro-rotors for reconfigurable hydrodynamic manipulation,” *Nat Commun* **10**, 1215 (2019).
- ⁴F. Schmidt, A. Magazzù, A. Callegari, L. Biancofiore, F. Cichos, and G. Volpe, “Microscopic engine powered by critical demixing,” *Physical Review Letters* **120**, 068004 (2018).
- ⁵J. Wang, “Cargo-towing synthetic nanomachines: towards active transport in microchip devices,” *Lab on a Chip* **12**, 1944–1950 (2012).
- ⁶M. Guix, C. C. Mayorga-Martinez, and A. Merkoçi, “Nano/micromotors in (bio) chemical science applications,” *Chemical reviews* **114**, 6285–6322 (2014).
- ⁷N. Pellicciotta, O. S. Bagal, V. C. Sosa, G. Frangipane, G. Vizsnyiczai, and R. D. Leonardo, “Light controlled biohybrid microbots,” *Advanced Functional Materials* , 2214801 (2023).
- ⁸L. Soler, V. Magdanz, V. M. Fomin, S. Sanchez, and O. G. Schmidt, “Self-propelled micromotors for cleaning polluted water,” *ACS nano* **7**, 9611–9620 (2013).
- ⁹M. Safdar, J. Simmchen, and J. Jänis, “Light-driven micro- and nanomotors for environmental remediation,” *Environ. Sci.: Nano* **4**, 1602–1616 (2017).
- ¹⁰A. Walther and A. H. Müller, “Janus particles,” *Soft matter* **4**, 663–668 (2008).
- ¹¹F. Merkt, A. Erbe, and P. Leiderer, “Capped colloids as light-mills in optical traps,” *New Journal of Physics* **8**, 216 (2006).
- ¹²H. Moyses, J. Palacci, S. Sacanna, and D. G. Grier, “Trochoidal trajectories of self-propelled janus particles in a diverging laser beam,” *Soft Matter* **12**, 6357–6364 (2016).
- ¹³S. Nedev, S. Carretero-Palacios, P. Kühler, T. Lohmüller, A. S. Urban, L. J. Anderson, and J. Feldmann, “An optically controlled microscale elevator using plasmonic janus particles,” *ACS photonics* **2**, 491–496 (2015).

- ¹⁴O. Ilic, I. Kaminer, Y. Lahini, H. Buljan, and M. Soljacic, “Exploiting optical asymmetry for controlled guiding of particles with light,” *Acs Photonics* **3**, 197–202 (2016).
- ¹⁵H.-R. Jiang, N. Yoshinaga, and M. Sano, “Active motion of a Janus particle by self-thermophoresis in a defocused laser beam,” *Phys. Rev. Lett.* **105**, 268302 (2010).
- ¹⁶S. Palagi, D. P. Singh, and P. Fischer, “Light-controlled micromotors and soft microrobots,” *Advanced Optical Materials* **7**, 1900370 (2019).
- ¹⁷I. Buttinoni, L. Caprini, L. Alvarez, F. J. Schwarzendahl, and H. Löwen, “Active colloids in harmonic optical potentials (a),” *Europhysics Letters* **140**, 27001 (2022).
- ¹⁸G. Tkachenko, V. G. Truong, C. L. Esporlas, I. Sanskriti, and S. Nic Chormaic, “Evanescent field trapping and propulsion of janus particles along optical nanofibers,” *Nature Communications* **14**, 1691 (2023).
- ¹⁹D. Fan, F. Q. Zhu, X. Xu, R. C. Cammarata, and C. Chien, “Electronic properties of nanoentities revealed by electrically driven rotation,” *Proceedings of the National Academy of Sciences* **109**, 9309–9313 (2012).
- ²⁰W. Gao, D. Kagan, O. S. Pak, C. Clawson, S. Campuzano, E. Chuluun-Erdene, E. Shipton, E. E. Fullerton, L. Zhang, E. Lauga, *et al.*, “Cargo-towing fuel-free magnetic nanoswimmers for targeted drug delivery,” *small* **8**, 460–467 (2012).
- ²¹P. Jones, O. Maragò, and G. Volpe, *Optical tweezers* (Cambridge University Press Cambridge, 2015).
- ²²G. Volpe, O. M. Marago, H. Rubinsztein-Dunlop, G. Pesce, A. Stilgoe, G. Volpe, G. Tkachenko, V. G. Truong, S. Nic Chormaic, F. Kalantarifard, *et al.*, “Roadmap for optical tweezers 2023,” *Journal of Physics: Photonics* (2023).
- ²³Y. Arita, M. Mazilu, and K. Dholakia, “Laser-induced rotation and cooling of a trapped microgyroscope in vacuum,” *Nature communications* **4**, 2374 (2013).
- ²⁴M. Friese, J. Enger, H. Rubinsztein-Dunlop, and N. R. Heckenberg, “Optical angular-momentum transfer to trapped absorbing particles,” *Physical Review A* **54**, 1593 (1996).
- ²⁵M. E. Friese, T. A. Nieminen, N. R. Heckenberg, and H. Rubinsztein-Dunlop, “Optical alignment and spinning of laser-trapped microscopic particles,” *Nature* **394**, 348–350 (1998).
- ²⁶N. Simpson, K. Dholakia, L. Allen, and M. Padgett, “Mechanical equivalence of spin and orbital angular momentum of light: an optical spanner,” *Optics letters* **22**, 52–54 (1997).
- ²⁷G. Pesce, G. Volpe, O. M. Maragó, P. H. Jones, S. Gigan, A. Sasso, and G. Volpe, “Step-by-step guide to the realization of advanced optical tweezers,” *JOSA B* **32**, B84–B98 (2015).

- ²⁸P. Galajda and P. Ormos, “Complex micromachines produced and driven by light,” *Applied Physics Letters* **78**, 249–251 (2001).
- ²⁹A. A. R. Neves, A. Camposeo, S. Pagliara, R. Saija, F. Borghese, P. Denti, M. A. Iatì, R. Cingolani, O. M. Maragò, and D. Pisignano, “Rotational dynamics of optically trapped nanofibers,” *Optics express* **18**, 822–830 (2010).
- ³⁰A. Magazzù, D. B. Ciriza, A. Musolino, A. Saidi, P. Polimeno, M. Donato, A. Foti, P. Gucciardi, M. Iatì, R. Saija, *et al.*, “Investigation of dust grains by optical tweezers for space applications,” *The Astrophysical Journal* **942**, 11 (2022).
- ³¹Y. Zong, J. Liu, R. Liu, H. Guo, M. Yang, Z. Li, and K. Chen, “An optically driven bistable janus rotor with patterned metal coatings,” *ACS nano* **9**, 10844–10851 (2015).
- ³²M. Fränzl, S. Muinos-Landin, V. Holubec, and F. Cichos, “Fully steerable symmetric thermoplasmonic microswimmers,” *ACS nano* **15**, 3434–3440 (2021).
- ³³C. Maggi, F. Saglimbeni, M. Dipalo, F. De Angelis, and R. Di Leonardo, “Micromotors with asymmetric shape that efficiently convert light into work by thermocapillary effects,” *Nature communications* **6**, 7855 (2015).
- ³⁴A. Girot, N. Danné, A. Wurger, T. Bickel, F. Ren, J. Loudet, and B. Pouligny, “Motion of optically heated spheres at the water–air interface,” *Langmuir* **32**, 2687–2697 (2016).
- ³⁵J. Liu, H.-L. Guo, and Z.-Y. Li, “Self-propelled round-trip motion of janus particles in static line optical tweezers,” *Nanoscale* **8**, 19894–19900 (2016).
- ³⁶S. M. Mousavi, I. Kasianiuk, D. Kasyanyuk, S. K. Velu, A. Callegari, L. Biancofiore, and G. Volpe, “Clustering of janus particles in an optical potential driven by hydrodynamic fluxes,” *Soft matter* **15**, 5748–5759 (2019).
- ³⁷D. Paul, R. Chand, and G. P. Kumar, “Optothermal evolution of active colloidal matter in a defocused laser trap,” *ACS Photonics* **9**, 3440–3449 (2022).
- ³⁸X. Gao, Y. Wang, X. He, M. Xu, J. Zhu, X. Hu, X. Hu, H. Li, and C. Hu, “Angular trapping of spherical janus particles,” *Small Methods* **4**, 2000565 (2020).
- ³⁹A. Callegari, M. Mijalkov, A. B. Gököz, and G. Volpe, “Computational toolbox for optical tweezers in geometrical optics,” *JOSA B* **32**, B11–B19 (2015).
- ⁴⁰J. L. Anderson, “Colloid transport by interfacial forces,” *Annual Review of Fluid Mechanics* **21**, 61–99 (1989).
- ⁴¹D. Bronte Ciriza, A. Magazzù, A. Callegari, G. Barbosa, A. A. Neves, M. A. Iatì, G. Volpe, and O. M. Maragò, “Faster and more accurate geometrical-optics optical force calculation using

neural networks,” ACS Photonics (2022).